Geophysical Research Letters

RESEARCH LETTER
10.1029/2025GL119671

Effect of Submerged Vegetation on Water Surface Geometry and Air–Water Momentum Transfer

G. Foggi Rota[1], A. Chiarini[1,2], and M. E. Rosti[1]

[1]Complex Fluids and Flows Unit, Okinawa Institute of Science and Technology Graduate University, Onna, Japan, [2]Dipartimento di Scienze e Tecnologie Aerospaziali, Politecnico di Milano, Milano, Italy

Key Points:

- First resolved simulation of turbulent air–water flow over vegetation, with quasi-realistic fluid properties
- Submerged vegetation smooths the water surface, damping steep deformations and regularizing streamwise wave fronts
- Despite altered interface shape, air–water momentum transfer remains unchanged, with implications for models

Supporting Information:

Supporting Information may be found in the online version of this article.

Correspondence to:

M. E. Rosti,
marco.rosti@oist.jp

Citation:

Foggi Rota, G., Chiarini, A., & Rosti, M. E. (2026). Effect of submerged vegetation on water surface geometry and air–water momentum transfer. *Geophysical Research Letters*, *53*, e2025GL119671. https://doi.org/10.1029/2025GL119671

Received 27 SEP 2025
Accepted 15 DEC 2025

Author Contributions:

Conceptualization: G. Foggi Rota, A. Chiarini, M. E. Rosti
Data curation: G. Foggi Rota
Formal analysis: G. Foggi Rota
Funding acquisition: M. E. Rosti
Methodology: G. Foggi Rota, A. Chiarini, M. E. Rosti
Project administration: M. E. Rosti
Software: G. Foggi Rota, A. Chiarini, M. E. Rosti
Supervision: M. E. Rosti
Validation: G. Foggi Rota
Visualization: G. Foggi Rota
Writing – original draft: G. Foggi Rota
Writing – review & editing: G. Foggi Rota, A. Chiarini, M. E. Rosti

Abstract Understanding how submerged vegetation modifies the water surface is crucial for modeling momentum exchange between shallow waters and the atmosphere. In particular, quantifying its impact on the equivalent aerodynamic roughness of the water surface is essential for improved boundary-layer parameterization in oceanic and atmospheric models. In this Letter, we present fully resolved multiphase simulations of gravity-driven flow over a fully submerged vegetated bed, capturing the coupled dynamics of air, water, and individual plant stems, under quasi-realistic conditions (the air/water viscosity ratio is real, while the density ratio is reduced tenfold). Our results show that vegetation submerged for four times its height regularizes the water surface suppressing strong deformations and homogenizing streamwise-propagating wave fronts along the transversal direction. Despite these alterations, the equivalent roughness perceived by the overlying air flow remains unchanged. These findings clarify vegetation–surface interactions and provide quantitative insights for nature-based wave mitigation strategies and atmospheric boundary-layer modeling.

Plain Language Summary The interaction between water and air at the surface of oceans, lakes, and rivers controls how gases like carbon dioxide and water vapor, as well as energy, are exchanged between the Earth's surface and the atmosphere. In coastal regions, where aquatic plants such as seagrass are common, these interactions become more complex. Scientists and engineers need accurate ways to describe how submerged vegetation affects the roughness of the water surface and the motion of air above it to improve climate and weather models. In this study, we use high-resolution computer simulations to investigate water flow over submerged vegetation, capturing the motion of water around individual plant stems and of the air above. We compare this case to an equivalent setup without vegetation. We find that while the water surface appears smoother and more regular along the direction transversal to the flow when vegetation is present, it generates essentially the same drag on the airflow. These findings support the use of submerged vegetation in coastal protection strategies designed to reduce wave impact, and they help refine atmosphere–ocean models.

1. Introduction

Fluvial and coastal flows are often characterized by shallow layers of turbulent water moving over heterogeneous beds—ranging from smooth sand to rocky substrates, to complex surfaces covered with aquatic vegetation. Vegetated beds, or aquatic *canopies*, play a critical role in limiting bed erosion (Zhao & Nepf, 2021), modulating flow dynamics (Ghisalberti & Nepf, 2004), and sustaining ecologically vital habitats (Duarte et al., 2020). Their hydrodynamic impact has been extensively studied over the past decades (Nepf, 2012).

A fundamental distinction exists between emergent and fully submerged canopies. Emergent vegetation, such as mangrove forests, interacts with both the water column and the air–water interface, influencing wave propagation and surface morphology (Mei et al., 2011; Mossa & De Padova, 2025). Owing to their complexity, these systems are often studied through laboratory and field experiments (Liu et al., 2008; van Rooijen et al., 2018; Wu & Cox, 2015; Zhu & Chen, 2019). In contrast, fully submerged canopies interact solely with the water column. Dense vegetation slows near-bed flow and generates a turbulent mixing layer at the canopy tip (Ghisalberti & Nepf, 2002; Nepf & Vivoni, 2000), where shear-driven turbulence replaces that generated by bed friction.

Much of our current understanding of submerged canopy flows derives from laboratory experiments (Ghisalberti & Nepf, 2006; Poggi et al., 2004; Tang et al., 2025) and fully resolved numerical simulations in open-channel configurations (Foggi Rota, Monti, et al., 2024; H. D. Kim et al., 2024; Löhrer & Fröhlich, 2023; Monti et al., 2019). In both approaches, the air-water interface is typically neglected or idealized as a flat, frictionless boundary. Consequently, models have largely focused on vegetation-induced drag (Etminan et al., 2017) and

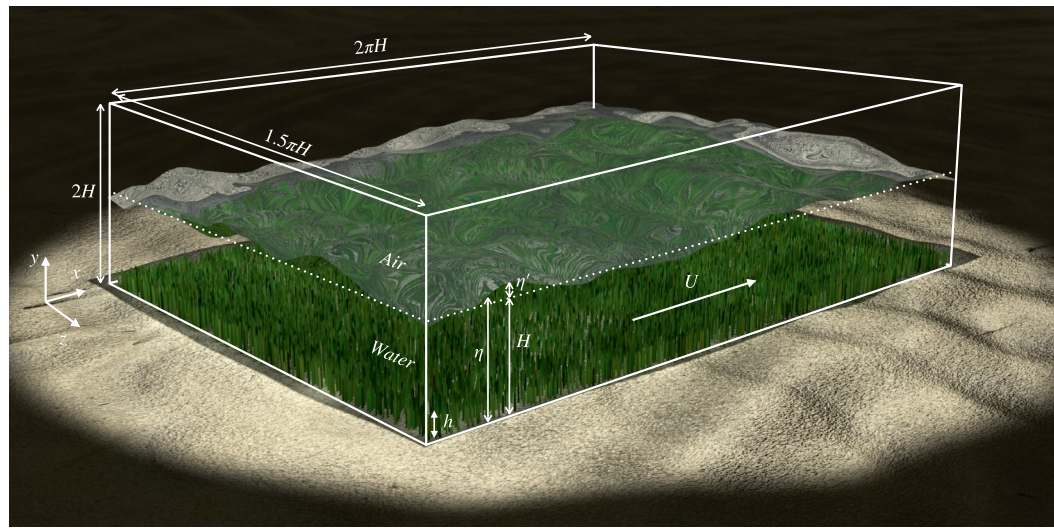

Figure 1. Simulation setup, showing the individually resolved stems of the submerged canopy and the turbulent air–water interface above. Relevant variables and parameters are sketched over an instantaneous realization of the system. Simulations capture the coupled dynamics of air and water, influenced by vegetation, to quantify how submerged canopies modify interface deformation.

subsurface mixing processes (Marjoribanks et al., 2017), leaving the influence of vegetation on the air-water interface largely unexplored.

Yet the air-water interface remains dynamically coupled to the turbulence beneath. The extent to which submerged vegetation alters interface morphology and modulates momentum exchange with the atmosphere remains poorly quantified. This gap is particularly significant for atmospheric modeling, where surface roughness defines the lower boundary condition for turbulent momentum flux in the atmospheric boundary layer (Hwang, 2022; Toba, 1972). Understanding whether—and how—submerged vegetation modifies this roughness is therefore essential for accurately representing air-sea interactions in large-scale geophysical simulations (Drennan et al., 2005; Yang et al., 2013).

In this study, we investigate the influence of submerged vegetation on the water surface in quasi-realistic conditions using fully resolved numerical simulations that simultaneously capture air and water flows, a deformable air-water interface, and the detailed geometry of individual plant stems (Figure 1). By comparing vegetated and smooth-bed cases under identical forcing, we show that vegetation significantly enhances surface deformation. Crucially, however, the overlying airflow remains largely unaffected. We further quantify the effective aerodynamic roughness length of the water surface as perceived by the atmospheric flow. These results have direct implications for understanding air-water coupling in vegetated systems, informing nature-based coastal protection strategies (Foggi Rota, Chiarini, & Rosti, 2025b; Kobayashi et al., 1993; Zhang & Nepf, 2021; Zhu et al., 2022), and improving atmospheric boundary layer modeling.

2. Numerical Methods

We perform simulations in a three-dimensional domain of length $2\pi H$, height $2H$, and width $1.5\pi H$ along the x, y, and z axes, respectively (Figure 1), according to established numerical practice for canopy flows (Monti et al., 2023; Sathe & Giometto, 2024). The domain is inclined at an angle $\Phi \approx 7°$ relative to the vertical gravity vector $\mathbf{g}$. The lower half ($y \leq H$) is filled with water, the upper half ($y \geq H$) with air, placing the undeformed interface at $y = H$. No-slip, no-penetration conditions are imposed at the bottom wall, while the top boundary is free-slip. Periodic boundary conditions are applied in the horizontal directions. The gravitational incline drives a net flow along the positive x direction in both fluid layers, equivalently to the imposition of a pressure gradient along the streamwise direction. This configuration mimics the action of a wind aligned with the underlying current.

Table 1
Relevant Flow Parameters for the Two Simulated Scenarios

	Re	Fr	We	μ_w/μ_a	ρ_w/ρ_a	N_s
Smooth bed	1,000	3	6	55	80	0
Vegetated bed	1,000	3	6	55	80	15,552

The motion of the fluid is governed by the incompressible Navier–Stokes equations:

$$\nabla \cdot \mathbf{u} = 0, \quad \frac{\partial \mathbf{u}}{\partial t} + \nabla \cdot (\mathbf{u}\mathbf{u}) = \frac{1}{\rho_f}(-\nabla p + \nabla \cdot \boldsymbol{\tau}) + \sigma k \delta_s \mathbf{n} + \mathbf{f}_{\mathrm{IBM}} + \mathbf{g}, \qquad (1)$$

where $\mathbf{u}$ and p are the velocity and pressure fields, ρ_f is the local fluid density (equal to ρ_w in water and ρ_a in air), $\boldsymbol{\tau}$ is the viscous stress tensor, and further terms to the right represent body forces. Velocity is continuous across the air–water interface, while the stresses exhibit a jump due to surface tension. This effect is modeled as a volumetric force of the form $\sigma k \delta_s \mathbf{n}$ (Popinet, 2018), where σ is the surface tension, k the local curvature, $\mathbf{n}$ the normal vector, and δ_s a Dirac delta function concentrated at the interface. We also introduce a body force $\mathbf{f}_{\mathrm{IBM}}$ to account for the effect of vegetation elements.

The vegetated bed consists of $N_s = 15552$ cylindrical rigid stems of length $h = 0.25H$ and diameter $d \approx 2 \times 10^{-2}H$, arranged semi-randomly to avoid preferential flow channeling (Foggi Rota, Monti, et al., 2024). To do so, we divide the bed into a grid of $n_x \times n_z = 144 \times 108$ rectangular tiles of area $\Delta S^2 = (2\pi H/n_x) \times (1.5\pi H/n_z)$, and randomly place each stem within each tile sampling a uniform distribution as in Monti et al. (2023). This tiling differs from the numerical grid and it is employed only to achieve the desired distribution of the stems, almost isotropic on the scale of the domain. The tips of the stems lay $3h$ under the water surface, at an "intermediate" submergence level which is not deep nor shallow, where the vegetation effect on the surface is not trivially expectable. Furthermore, the configuration considered produces a dense canopy (Monti et al., 2020) occupying approximately 4% of the total simulation volume (air plus water), which thus yields a marked modulation on the flow. Vegetation–fluid coupling is enforced via a no-slip condition using a force distribution $\mathbf{f}_{\mathrm{IBM}}$ computed through a Lagrangian immersed boundary method (IBM) (Foggi Rota, Koseki, et al., 2024; Huang et al., 2007; Olivieri et al., 2020). Each stem is discretized with 126 uniformly distributed Lagrangian markers. Additional implementation details are provided in the Supporting Information of Foggi Rota, Koseki, et al. (2024).

Air and water phases are distinguished by a color function related to the volume-of-fluid (VOF) field $\phi(\mathbf{x}, t)$ through cell averaging. This enables a monolithic formulation of Equation 1, with fluid properties weighted by ϕ in each cell. The stress tensor is therefore computed as $\boldsymbol{\tau} = \mu_f(\nabla \mathbf{u} + \nabla \mathbf{u}^T)$, where $\mu_f(\mathbf{x}, t)$ is the local dynamic viscosity.

The system is characterized by several key dimensionless parameters, summarized in Table 1. Decomposing the gravity vector $\mathbf{g}$ into components parallel and normal to the bed, g_x and g_y, we define a gravity-driven velocity scale $U = \sqrt{g_x H}$ analogous to the friction velocity $u_\tau = \sqrt{\tau_w/\rho_f}$ in wall-bounded turbulence (J. Kim et al., 1987), where the wall shear stress τ_w balances a driving pressure gradient along the streamwise direction. The inclination angle of the domain is then $\Phi = \arctan(g_x/g_y)$. The Reynolds number is defined as $\mathrm{Re} = \rho_w U H/\mu_w$, where μ_w is the dynamic viscosity of water—in its turn, analogous to the friction Reynolds number. We set $\mathrm{Re} \approx 1000$ by adjusting g_x to ensure fully turbulent conditions. The Froude number is fixed at $Fr = U/\sqrt{g_y H} \approx 3$ by appropriately selecting g_y. Surface tension is chosen to yield a Weber number $We = \rho_w U^2 H/\sigma \approx 1$, as in Giamagas et al. (2023). The viscosity ratio is set to its physical value, $\mu_w/\mu_a = 55$, and a density ratio of $\rho_w/\rho_a = 80$ is imposed. While this density ratio is high for the practice of fully resolved simulations, where higher values lead to numerical instabilities, it is still tenfold away from reality. An increase in the density ratio would likely affect the results quantitatively, but we can expect the changes to be minor and with no qualitative or phenomenological modifications. In fact, studies on bubble dynamics (Jain et al., 2019) have shown that limiting behaviors emerge for density ratios exceeding $\mathcal{O}(100)$. Moreover, in interfacial flows it is typically the Atwood number (Rigon et al., 2021), rather than the density ratio itself, that governs inertia contrast. The Atwood number is defined as $A = (\rho_w - \rho_a)/(\rho_w + \rho_a)$, which in our simulations equals $A = 0.975$, only 2% smaller than the realistic $A = 0.997$. Saturation is commonly observed for $A \gtrsim 0.94$ in the study of interfacial instabilities (Burton, 2011). Furthermore, our numerical setup compares well with the experiments of Shimizu et al. (1992), performed in a canopy fully submerged in water with a free air-water interface above. In validating our solver, we carried out simulations in the water domain with a flat free-slip boundary at the top (full details are provided in the Supporting Information S1). The good agreement between these simulations and the experimental results confirms that our

computations are performed in a regime where further increasing the inertia contrast at the interface plays a limited role.

We solve Equation 1 using our in-house, well-validated solver *Fujin* (https://www.oist.jp/research/research-units/cffu/fujin). Spatial derivatives are computed using second-order central finite differences, and time integration is performed with a second-order Adams–Bashforth scheme. Incompressibility is enforced via a projection–correction method (J. Kim & Moin, 1985), where the pressure Poisson equation is solved efficiently using the *2decomp* domain decomposition library, coupled with an in-place spectral solver based on Fourier series (Dorr, 1970). The volume-of-fluid (VOF) method adopts the multidimensional tangent of hyperbola for interface capturing (MTHINC) formulation by Ii et al. (2012), which has been validated against analytical benchmarks (Rosti et al., 2019) and applied in several recent studies (Cannon et al., 2024; De Vita et al., 2021; Hori et al., 2023).

Flow variables are discretized on a staggered Cartesian grid with 1,152 uniform points in the streamwise (x) direction and 864 in the spanwise (z) direction. In the wall-normal (y) direction, 480 non-uniform grid points are used, to resolve the bottom-wall boundary layer and to maintain nearly isotropic cells near the air-water interface. This resolution is sufficient to accurately capture both smooth and vegetated bed cases, as demonstrated in prior studies (Foggi Rota, Monti, et al., 2024; Monti et al., 2023). We have also verified that doubling the resolution does not significantly alter the results. Each of the two simulations presented in this study was performed on 7,200 Fujitsu A64FX CPUs of the supercomputer Fugaku at RIKEN (https://www.r-ccs.riken.jp/en/fugaku/) for approximately three months: the first two months required to reach a fully developed turbulent state after a transient of $24\sqrt{H/g}$, and the final month spent to collect sufficient statistics over $12\sqrt{H/g}$ time units, every $0.06\sqrt{H/g}$ for the fluid and every $0.6\sqrt{H/g}$ for the interface. Integration was performed with a time-step of $1.2 \cdot 10^{-5}\sqrt{H/g}$, and a total of 25,000,000 core-hours were employed for this project.

3. Results

3.1. Interface Morphology

A fully turbulent flow develops in our setup (see Supporting Information S1 for further details) with velocity fluctuations in the water sustained either by the near-wall turbulent cycle over the smooth bed (Jiménez & Pinelli, 1999) or by the shear layer at the canopy tip (Nepf, 2012). This behavior is evident from the flow visualizations shown in panels (a) and (b) of Figure 2, where characteristic velocity streaks—central to the wall turbulence cycle—are observed near the smooth bed. Over the vegetated bed, by contrast, turbulence is dominated by Kelvin–Helmholtz rollers generated by the drag discontinuity at the canopy tip (Finnigan, 2000; Foggi Rota, Monti, et al., 2024). In Figure 2 we isolate them as negative iso-surfaces of the pressure field smoothened with a box filter, following the same approach of our former study (Foggi Rota, Tressoldi, et al., 2025). The turbulent fluctuations deform the air-water interface and propagate into the air layer, which exhibits sweep and ejection events respectively defined as flow regions where $u' > 0, v' < 0$ or $u' < 0, v' > 0$, with u'/v' the streamwise/vertical velocity fluctuations. Fluctuation intensity peaks just above the interface and decays with height. The interface responds by bending and deforming under the action of turbulence, resulting in a complex and dynamic morphology that we aim to characterize.

We compare flows over smooth and vegetated bed at fixed value of Re_f, aiming to isolate the effect of vegetation on the flow established over an otherwise unmodified incline. Vegetation on the bed significantly alters the flow. Canopy drag reduces the mean velocity of the water, $U_{b,w}$, thereby decreasing the slip velocity at the interface, U_{int} (defined as the mean flow velocity at the average interface position $y = H$). As a result, the overlying air flow also slows down, with a corresponding reduction in its mean velocity, $U_{b,a}$. These values are summarized in Table 2.

The vegetation considered in this study is rigid, while natural vegetation is typically flexible and therefore reconfigures (Alben et al., 2002) and oscillates (Foggi Rota, Koseki, et al., 2024) under the action of the incoming turbulent flow. We thus forecast quantitative differences from our results in realistic environments, while the underlying physics should remain unchanged. Flexible stems, in facts, tend to assume a streamlined posture when they deflect (proportionally to their flexibility), thereby shielding the flow inside the canopy from the turbulent fluctuations above. The variable configuration of flexible stems diffuses the drag discontinuity generated at their tips, leading to weaker Kelvin–Helmholtz rollers compared to the rigid case and to an overall reduction in turbulence intensity in the outer flow (Foggi Rota, Monti, et al., 2024; Monti et al., 2023). Thus, while stem

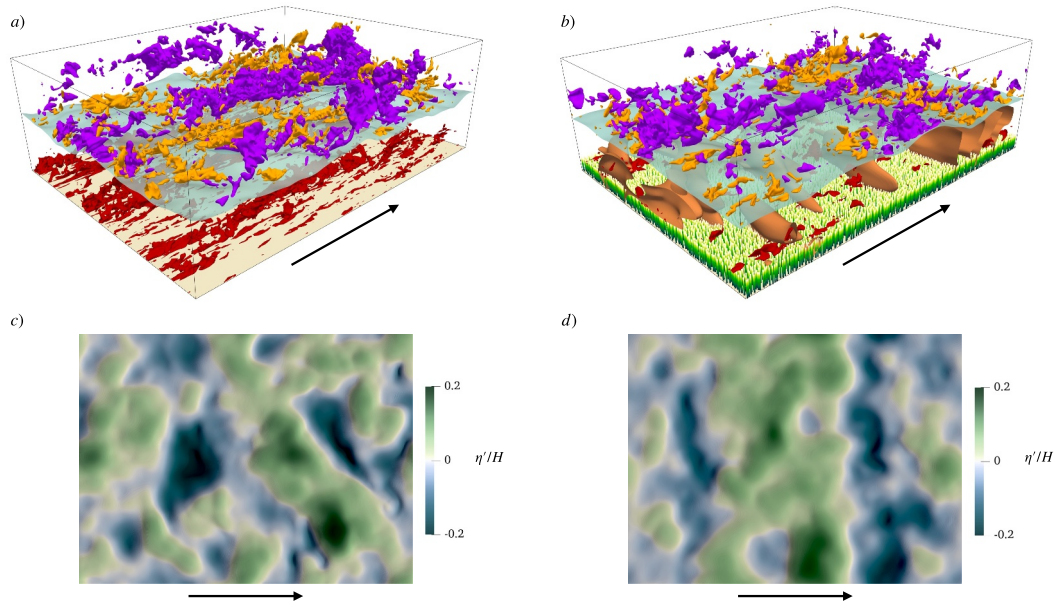

Figure 2. Visualizations of the turbulent structures (panels a, b) and interface deformation (panels c, d) above the smooth and vegetated bed in the left and right panels, respectively. In (a, b), red iso-surfaces denote regions of high streamwise velocity in the water, while in the air orange iso-surfaces correspond to fast fluid moving toward the interface and purple iso-surfaces to slow fluid rising upward. In (b) we also isolate Kelvin-Helmholtz rollers in the water as brown iso-surfaces of the filtered pressure field (see main text for details). In (c, d) we color interface fluctuations from $-0.2H$ to $0.2H$ seen from the top with a linear colormap ranging from blue to green, with white at null values. The interface appears qualitatively more rippled in the smooth bed case, while in the vegetated bed case we appreciate the spanwise regularization of streamwise–propagating wave fronts over the underlying rollers.

flexibility significantly affects the flow inside the canopy, it leaves the outer turbulence attenuated but structurally similar. Since in our simulations the interaction between submerged vegetation and the water surface is primarily mediated by outer-flow turbulence, we choose to focus on the conditions where that turbulence is most intense and to consider rigid vegetation stems.

Flow modulation by the vegetated bed leads to markedly different interface states. Denoting the interface elevation from the bottom wall as $\eta(x,z;t)$, conservation of the two fluid phases requires that its mean value satisfies $\langle\eta\rangle = H$, where the operator $\langle\cdot\rangle$ denotes averaging over time and the homogeneous x and z directions. We therefore define the interface fluctuations as $\eta'(x,z;t) = \eta(x,z;t) - H$. This decomposition is illustrated in Figure 1. Visualizations in panels (c) and (d) of Figure 2 show that the interface appears more rippled over the smooth bed, while in the vegetated case, fluctuations are more homogeneous in the spanwise direction. To quantify this, Table 2 reports the root-mean-square (rms) of η', which remains nearly unchanged between the two cases. However, the rms of its spatial gradients, $\partial_i\eta'$ with $i \in \{x,z\}$, reveals clear differences. Both gradients are attenuated over the vegetated bed, with the strongest reduction occurring in the spanwise (z) direction—consistent with the streamwise–propagating wavefronts observed in the visualizations. We further introduce a characteristic length-scale, l_x, defined as the first zero–crossing of the autocorrelation function $C_{\eta,x}(\delta) = \langle\eta(x,z;t)\,\eta(x+\delta,z;t)\rangle/\langle\eta'^2\rangle$, and measure $l_x \approx 1.2H$ in the vegetated bed case: a value 40% larger than in the smooth bed case

Table 2
Flow Measurements and Scalar Indicators of the Interface Morphology, as Introduced in the Text

	$U_{b,w}/U$	$U_{b,a}/U$	U_{int}/U	$\sqrt{\langle\eta'^2\rangle}$	$\sqrt{\langle\partial_x\eta'^2\rangle}$	$\sqrt{\langle\partial_z\eta'^2\rangle}$	$\langle\mathcal{K}\rangle$
Smooth bed	20.29	32.67	24.67	0.07	0.23	0.19	0.25
Vegetated bed	4.95	18.29	10.24	0.07	0.20	0.14	0.31

Note. Reported values are robust and converged, as they exhibit a variation less then ~5% upon halving the time history used for their computation.

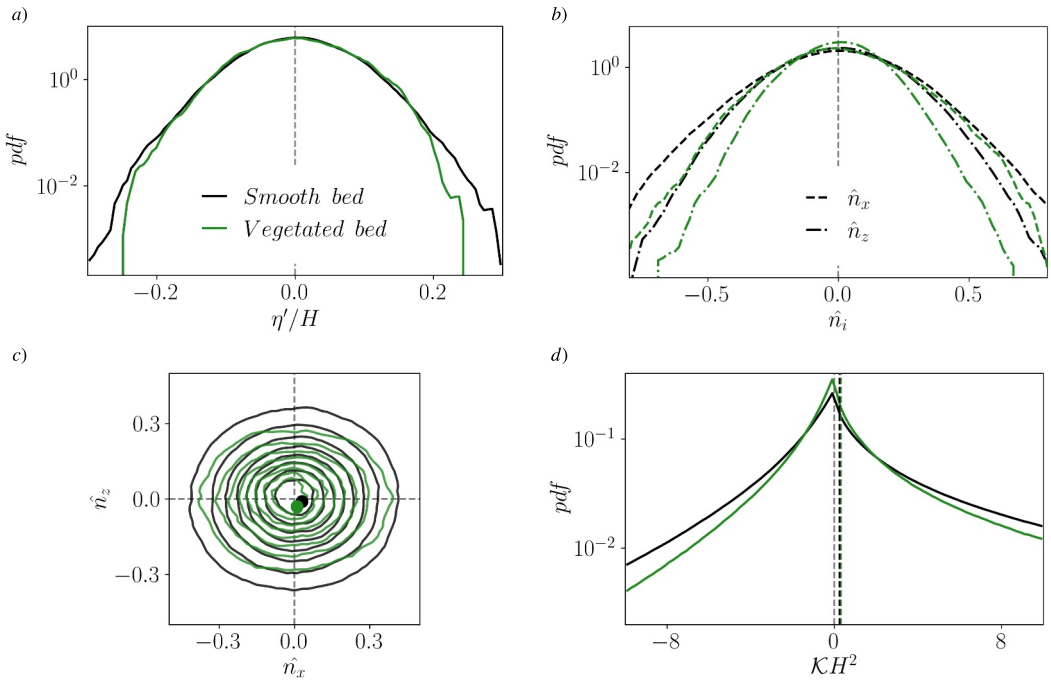

Figure 3. Characterization of the interface deformation. Panel (a) shows the probability density function of the interface elevation, while panel (b) refers to the different components of the surface normal $\hat{n}$, oriented upward. In panel (c) we present the joint probability density function of the normal components along the streamwise and spanwise directions, while in panel (d) we report the distribution of the Gaussian curvature $\mathcal{K}$. Vegetation preferentially alters interface deformation along the transverse direction, reducing intense fluctuations.

which confirms the interface regularization by vegetation and might be interpreted as the typical wavelength of the streamwise–propagating wavefronts mentioned above. Interestingly, although the canopy stems are almost isotropically distributed in the x–z plane, the flow breaks this isotropy: submerged vegetation affects the interface differently along each direction. The spanwise regularization is likely linked to increased coherence of the underlying turbulent structures, particularly the formation of Kelvin–Helmholtz rollers (Finnigan, 2000).

Further insight is provided by the probability density functions (PDFs) of the interface fluctuations. As shown in panel (a) of Figure 3, the distributions of η' overlap at moderate amplitudes but diverge in the tails: the vegetated bed case consistently shows lower probabilities of large excursions, indicating a suppression of extreme interface deformations.

The surface gradients can be expressed through the surface-normal unit vector $\hat{\mathbf{n}} = \{\hat{n}_x, \hat{n}_y, \hat{n}_z\} = \{\partial_x\eta', 1, \partial_z\eta'\}/\sqrt{1 + \partial_x\eta'^2 + \partial_z\eta'^2}$, pointing upward form the interface into the air. The distributions of its components are shown in panel (b) of Figure 3. The effect of vegetation is most evident in the spanwise component $\hat{n}_z$, where the probability of steep interface slopes is markedly reduced. This trend is further confirmed by the joint PDF of $\hat{n}_x$ and $\hat{n}_z$ shown in panel (c): while the smooth-bed case exhibits nearly circular isolines, the vegetated case appears compressed along the $\partial_z\eta'$ axis, reinforcing the anisotropic modulation of interface shape induced by submerged vegetation.

Additionally, we characterize the shape of the interface by computing its Gaussian curvature, $\mathcal{K}$, expressed as the ratio of the determinants of the second and first fundamental forms, $\mathcal{K} = \det(\mathrm{II})/\det(\mathrm{I})$ (Gauss, 1828), and show it in panel (d) of Figure 3. At each point on the interface and at every time instant, $\mathcal{K}$ is defined as the product of the principal curvatures, κ_1 and κ_2, corresponding to the maximum and minimum curvatures of surface cross-sections taken in planes containing the local surface normal $\hat{\mathbf{n}}$. The distribution of $\mathcal{K}$ is skewed and exhibits a slightly positive mean (indicated by the colored vertical lines in panel (d) and reported in Table 2), suggesting a predominance of dome-like deformations over saddle-like ones. However, the PDFs peak near zero curvature,

consistent with the presence of propagating wavefronts characterized by one vanishing principal curvature ($\kappa_2 = 0$). As with other metrics, vegetation reduces the frequency of high-curvature events.

We therefore conclude that the vegetated bed significantly influences the interface geometry, as evidenced by the visualizations in Figure 2, globally suppressing intense deformations and regularizing streamwise-traveling wavefronts in the transverse direction. This finding is consistent with the preferential spanwise orientation of turbulent structures observed over vegetation canopies (Finnigan, 2000).

3.2. Momentum Transfer to the Overlaying Air Flow

A conventional approach to quantify the dynamical influence of an irregular surface on the overlying turbulent flow—and thus the momentum transfer across the interface—is through the concept of *equivalent roughness*, originally developed in the context of wall-bounded turbulence. The idea is to relate the effective roughness of a complex surface to that of the canonical experiments by Nikuradse (1933), who measured flow resistance in pipes roughened with uniform spherical sand grains. Here, we extend this concept to assess whether the submerged canopy modifies the momentum exchange between water and air across the deformable interface.

The classical framework for describing momentum transfer near a boundary is based on the logarithmic law of the wall (Pope, 2000), or simply log-law, which characterizes the mean velocity profile of a fully developed turbulent flow above a smooth wall:

$$\langle u^+ \rangle = \frac{1}{\kappa} \log \tilde{y}^+ + B, \tag{2}$$

where $\langle u^+ \rangle = \langle u \rangle / u_\tau$ is the mean velocity expressed in viscous units, $u_\tau = \sqrt{\tau_w / \rho_f}$ is the friction velocity defined from the wall shear stress $\tau_w = \mu_f \mathrm{d}\langle u \rangle / \mathrm{d}|_y = 0$, and $\tilde{y}^+ = \tilde{y}/\delta_\nu$, with $\tilde{y}$ the distance from the wall and $\delta_\nu = \mu_f / \left(\rho_f u_\tau\right)$ the viscous length scale. The constants $\kappa \approx 0.41$ and $B \approx 5.2$ are empirically determined. To account for surface roughness, the log-law can be reformulated using the concept of equivalent sand-grain roughness, denoted k_s^+ (Jiménez, 2004), to rescale the $\tilde{y}^+$ coordinate. The quantity k_s^+ represents the radius of Nikuradse-type roughness elements that would produce the same mean velocity profile as the actual surface, thus serving as a dynamical measure of surface-induced momentum transfer. In this case, the velocity profile becomes:

$$\langle u^+ \rangle = \frac{1}{\kappa} \log\left(\frac{\tilde{y}^+}{k_s^+}\right) + \tilde{B}\left(k_s^+\right) \tag{3}$$

where $\tilde{B}$ is a roughness-dependent function obtained from Nikuradse's experiments. The limit $k_s^+ \to 0$ corresponds to a hydraulically smooth wall, with $\tilde{B} \to B + (1/\kappa)\log\left(k_s^+\right)$ and recovering Equation 2. Conversely, in the fully rough regime, $k_s^+ \to \infty$ and $\tilde{B}$ tends toward an universal constant B_2. When the roughness is irregular or non-uniform–as in the case of a deformable interface—k_s^+ no longer directly reflects geometric features but remains a meaningful dynamical parameter: it quantifies the effective momentum exchange between the surface and the overlying flow. Variants of this quantity are widely used in geophysical applications, where specifying the equivalent roughness of the water surface is critical for defining lower boundary conditions in atmospheric and oceanic models (Drennan et al., 2005; Yang et al., 2013). Assuming that the turbulent air flow over the water surface occurs in the fully rough regime, we adopt the modified form of the log-law considered by Yoshimura et al. (2024) to quantify momentum transfer across the air/water interface,

$$\langle \Delta u^+ \rangle = \frac{1}{\kappa} \log \frac{\tilde{y} + y_s}{y_s}, \; y \geq H, \tag{4}$$

reliant on the single parameter y_s. Here, $\tilde{y} = y - H$, y_s plays the role of both a roughness length-scale and a vertical offset of the air flow origin over the surface, and $\langle \Delta u^+ \rangle = \langle \Delta u \rangle / u_\tau$ with $\langle \Delta u \rangle = \langle u \rangle - U_{\mathrm{int}}$ shifts the mean air velocity profile by the interface advection speed U_{int} to reflect the moving boundary. Unlike the case of a flat, rigid wall, the shear stress at the deformable interface is not solely due to viscous effects. The viscous shear stress, averaged across both water and air, is given by $\tau_\mu = \langle \mu_f \frac{\partial u}{\partial y} \rangle$. However, because velocity fluctuations at the

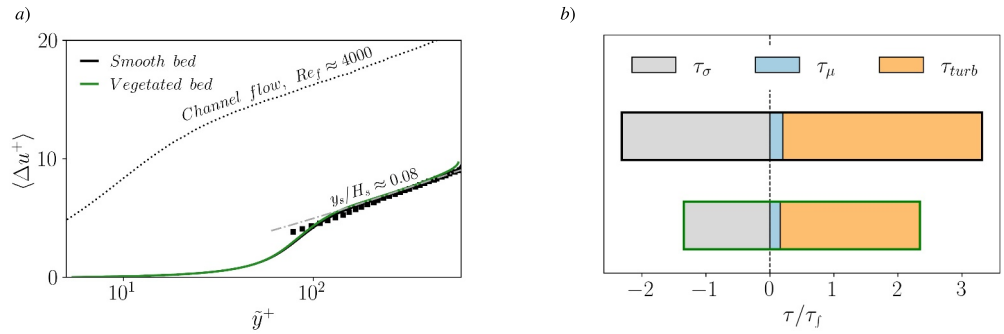

Figure 4. Characterization of the surface roughness. In panel (a) we report the mean profiles of the streamwise velocity in the air: the collapse of the two curves highlights the negligible effect of submerged vegetation on the air flow. Results from the simulations of Bernardini et al. (2014) over a flat rigid wall are reported as a dotted line, with the offset between those and our results quantifying the momentum deficit due to roughness. We report the fit with the log-law in Equation 4 as a gray dash-dotted line, and annotate the ratio between the equivalent roughness of the surface and the significant wave height above that. Our data are in good agreement with those of Sullivan et al. (2000), reported in panel (a) as black squares. In panel (b) we show the integrated components of the shear stress balance (from Equation 5 in the text).

interface are non-zero and surface tension contributes, two additional terms must be considered: the turbulent shear stress, $\tau_{\text{turb}} = -\langle \rho_f u' v' \rangle$, and the surface tension-induced stress (Rosti et al., 2019), defined as $\tau_\sigma = \int_0^y \langle \sigma k \delta_s n_x \rangle dy$. Thus, the total shear stress at any vertical location in the air is expressed as

$$\tau_{\text{tot}}(y) = \tau_\mu(y) + \tau_{\text{turb}}(y) + \tau_\sigma(y), \tag{5}$$

with no term vanishing at the interface $y = H$. We consequently generalize the friction velocity u_τ to be a local quantity varying with height, following the formalism of Monti et al. (2020):

$$u_\tau(y) = \sqrt{\frac{\tau_{\text{tot}}(y)}{\rho_f \left(2 - \frac{y}{H}\right)}}, \quad H \le y \le 2H. \tag{6}$$

This definition of u_τ is used to normalize the mean velocity profile in Equation 4. Note that the surface tension contribution τ_σ can be determined by enforcing closure of the shear balance in Equation 5 once the driving force for the air flow is specified.

We are now positioned to quantify the roughness length scale y_s in our setups. Under the scaling introduced above, the mean streamwise velocity profiles in the air collapse remarkably well for the cases with the smooth and the vegetated bed, as shown in panel (a) of Figure 4. This indicates that, despite the significant morphological changes of the interface discussed in the previous section, the submerged vegetation considered here does not appreciably modify the turbulent air flow above. The momentum loss due to surface roughness is evident from the downward shift of the logarithmic region relative to the flat rigid wall case (i.e., channel flow), and is quantitatively characterized by y_s, which we measure as $y_s/H \approx 0.022$ regardless of vegetation presence. Conventionally, y_s is expressed in terms of the *significant wave height* H_s, defined as the average height of the highest one-third of waves in a given area, measured crest to trough. Following Goda (1970), we estimate $H_s \approx 4\sqrt{\langle \eta'^2 \rangle} \approx 0.28H$ for both simulated scenarios, since $\sqrt{\langle \eta'^2 \rangle}$ remains essentially unchanged (see table 2). There follows $y_s/H_s \approx 0.08$, which lies close to the range reported by available field measurements (Drennan et al., 2005) and appears in remarkable agreement with the analytical prediction of Taylor and Yelland (2000) (further details in the Supporting Information S1). Alternatively, in the formalism of Equation 3 and assuming $\tilde{B} = 11.8$, we find $k_s^+ \approx 490$, confirming the former hypothesis of fully rough regime for which $k_s^+ \gtrapprox 100$ (Kadivar et al., 2021).

Our measurements in the logarithmic region align closely with those of Sullivan et al. (2000) (data were extracted from Figure 11 of their manuscript, for $c/u_* = 7.32$), shown as black squares in panel (a) of Figure 4, which they noted to lay at the threshold of the fully rough regime: a condition commonly encountered in geophysical flows (Kitaigorodskii & Donelan, 1984). Sullivan et al. (2000) studied air flow exclusively, using a Couette setup where

the velocity components at the water surface matched the irrotational orbital velocities of a two-dimensional deep-water gravity wave—a scenario markedly different from ours and, notably, unaffected by the air/water density ratio. Nevertheless, the close correspondence between their results and ours suggests that variations at the water surface as well as an increase of the density ratio have limited influence on the turbulent air flow within the logarithmic region.

The presence of the moving interface eliminates the conventional viscous region, where $\langle \Delta u^+ \rangle \approx y^+$ would typically hold. This peculiarity in our mean velocity profiles is better understood through the integral shear-stress balance, obtained by integrating Equation 5 from the interface to the top of the domain, yielding $\tau_{\int} = \int_H^{2H} (\tau_\mu(y) + \tau_{\text{turb}}(y) + \tau_\sigma(y))\, dy$. We analyze in panel (b) of Figure 4 the individual integral contributions normalized by $\tau_{\int}$, such that the histogram bars sum to unity. The viscous contribution τ_μ plays a marginal role, consistent with the disappearance of the viscous sublayer, while the interfacial contribution τ_σ balances the turbulent fluctuations τ_{turb}, justifying the rescaling introduced in Equation 6. Notably, τ_{turb}—and consequently τ_σ—is diminished in the vegetated case due to the reduced air flow over the interface, which moves at a lower velocity U_{int}, thereby lowering the effective Reynolds number of the air flow (see Supporting Information S1 for further details). Nevertheless, this modulation is fully accounted for by our rescaling, leading to overlapping velocity profiles across the investigated scenarios for the same value of y_s.

Turbulence generated at the canopy tip differs both qualitatively and quantitatively from that developing over the smooth bed, leading to distinct turbulent states in the water, which in turn imprint on the interface through the morphological modifications discussed in the previous section. However, introducing vegetation not only alters water-side turbulence, but also modifies the mean water flow, such that the air is exposed to a surface not only of different morphology, but also with different slip velocity. The framework we developed to rescale the mean flow profile of the air explicitly accounts for the change in slip velocity U_{int}, while recasting any residual dependence on interface morphology into the roughness length y_s. Remarkably, the finding that y_s remains unchanged between the vegetated and smooth-bed cases demonstrates that the modulation of air-side turbulence, measured by τ_{turb}, is entirely governed by the variation in slip, overshadowing the effects of the modest variation in the viscous shear stress τ_μ shown in panel b of Figure 4. In other words, interface slip sets the Reynolds number of the air flow over the interface. Upon introducing vegetation of the kind we considered, the interface slows down and turbulence is modulated according to the new Reynolds number, whose effect is accounted for by our rescaling. Compared to such effect, the role played by the modification of interface morphology, despite present, is negligible. We thus emphasize the critical role of the interface velocity U_{int} in the collapse of the mean velocity profiles $\langle \Delta u^+ \rangle$. Vegetation slows the water flow, which still exchanges approximately the same amount of streamwise momentum with the air as in the smooth bed case. As a result, the overlying air flow is also slower in the vegetated case. Given the similarity of the air-side velocity profiles, this reduction is fully captured by the velocity at the lower boundary of the air flow—the water surface. We report a reduction in U_{int} of approximately 40% between the smooth and vegetated bed scenarios. From a modeling perspective, even if changes in surface roughness y_s may be neglected, accurate knowledge of the interfacial velocity U_{int} remains essential. While estimating y_s requires detailed measurements of the air velocity profile in the logarithmic region—a challenging task—U_{int} can be readily obtained using simple experimental techniques, making it a more accessible and practical parameter for applications.

4. Discussion

We performed direct numerical simulations of two-phase turbulent flow over submerged vegetation, explicitly resolving both the air-water interface and all individual vegetation elements. These simulations approach realistic conditions and capture the essential dynamics of wave-current-vegetation interactions in aquatic environments.

We investigated the morphology of the water surface and the dynamics of the overlying air flow by comparing smooth-bed and vegetated-bed configurations under otherwise identical conditions. The key findings are as follows: (a) the presence of submerged vegetation significantly modifies the interface morphology, producing a geometrically smoother and more regular surface characterized by reduced curvature and surface gradients. In particular, interface fluctuations are noticeably regularized in the direction transverse to the mean flow; (b) strikingly, despite these pronounced morphological alterations, the momentum transfer to the air remains essentially unaffected. This is evident when the mean velocity profile is appropriately rescaled using the local

value of the total shear stress. Thus, for the fully rough interface conditions considered here—where the air flow develops at a moderate distance from the vegetation canopy (Kitaigorodskii & Donelan, 1984; Sullivan et al., 2000)—the impact of submerged vegetation on the equivalent aerodynamic roughness may be neglected for atmospheric modeling purposes. In this regime, the only essential fitting parameter required to accurately describe the air flow is the velocity of the water surface.

These results advance our understanding of how aquatic vegetation influences water surface morphology, with implications for both fundamental research in environmental fluid mechanics and practical applications, such as the development of vegetation-based strategies for coastal protection (Kobayashi et al., 1993; Lorenzo et al., 2023; Zhang & Nepf, 2021). Furthermore, by demonstrating the limited impact of submerged vegetation on the overlying air flow, this study provides valuable insights for atmospheric boundary-layer modeling.

Naturally, the scope of our work is limited to a specific configuration with a simple plant geometry at a fixed submergence level, and a density ratio between water and air lower than the real one (yet representative of a regime where the effect of the inertia contrast is saturated). While the computational demand of simulations prevents us from a broader exploration of the parameter space, we anticipate that our conclusions may not hold when vegetation is significantly closer to the interface, potentially coming in contact with it. Future work should investigate this case, aiming to identify vegetation that optimizes interface modulation for wave attenuation purposes. In fact, the present canopy mimics a dense meadow of plants composed of single rigid stems—a somewhat idealized scenario—whereas alternative geometries, including irregular or patchy distributions (Foggi Rota, Tressoldi, et al., 2025; Park & Nepf, 2025; Winiarska et al., 2024), may offer improved or tunable performance for nature-based coastal defenses. Additionally, natural vegetation is typically flexible, while our study only considers rigid plants. By doing so, we are able to clearly isolate the surface modulation induced by canopy-driven turbulence, while leaving open the question of any potential "resonant" interaction between surface waves and deflection waves within the canopy (i.e., *monami* waves, (Ackerman & Okubo, 1993)), to be explored in upcoming studies.

Inclusion in Global Research Statement

This research did not involve local communities, authorities, or field sites requiring permits or formal collaboration agreements. All data were generated through numerical simulations. The authors affirm their commitment to equitable research practices as outlined in the TRUST Code of Conduct.

Conflict of Interest

The authors declare no conflicts of interest relevant to this study.

Data Availability Statement

All data needed to evaluate the conclusions of this Letter are present in the main text and/or the Supporting Information S1. Processed data discussed in the text, used to generate figures and values reported in tables, are also made publicly available on Zenodo (Foggi Rota, Chiarini, & Rosti, 2025a): https://doi.org/10.5281/zenodo.17588891. Numerical simulations were carried out using a standard direct numerical simulation solver for the Navier–Stokes equations. Full details of the code implementation, validation, and related resources are available on the website of the Complex Fluids and Flows Unit at OIST (www.oist.jp/research/research-units/cffu/fujin).

Acknowledgments
The research was supported by the Okinawa Institute of Science and Technology Graduate University (OIST) with subsidy funding to M.E.R. from the Cabinet Office, Government of Japan. M.E.R. also acknowledges funding from the Japan Society for the Promotion of Science (JSPS), Grants 24K00810 and 24K17210. The authors acknowledge the computer time provided by the Scientific Computing and Data Analysis section of the Core Facilities at OIST and the computational resources offered by the HPCI System Research Project with Grants hp220402, hp240006, hp250035.

References

Ackerman, J. D., & Okubo, A. (1993). Reduced mixing in a marine macrophyte canopy. *Functional Ecology*, *7*(3), 305–309. https://doi.org/10.2307/2390209

Alben, A., Shelley, M., & Zhang, J. (2002). Drag reduction through self-similar bending of a flexible body. *Nature*, *420*(6915), 479–481. https://doi.org/10.1038/nature01232

Bernardini, M., Pirozzoli, S., & Orlandi, P. (2014). Velocity statistics in turbulent channel flow up to. *Journal of Fluid Mechanics*, *742*, 171–191. https://doi.org/10.1017/jfm.2013.674

Burton, G. C. (2011). Study of ultrahigh Atwood-number Rayleigh–Taylor mixing dynamics using the nonlinear large-eddy simulation method. *Physics of Fluids*, *23*(4), 045106. https://doi.org/10.1063/1.3549931

Cannon, I., Soligo, G., & Rosti, M. E. (2024). Morphology of clean and surfactant-laden droplets in homogeneous isotropic turbulence. *Journal of Fluid Mechanics*, *987*, A31. https://doi.org/10.1017/jfm.2024.380

De Vita, F., De Lillo, F., Bosia, F., & Onorato, M. (2021). Attenuating surface gravity waves with mechanical metamaterials. *Physics of Fluids*, *33*(4), 047113. https://doi.org/10.1063/5.0048613

Dorr, F. W. (1970). The direct solution of the discrete poisson equation on a rectangle. *SIAM Review*, *12*(2), 248–263. https://doi.org/10.1137/1012045

Drennan, W. M., Taylor, P. K., & Yelland, M. J. (2005). Parameterizing the sea surface roughness. *Journal of Physical Oceanography*, *35*(5), 835–848. https://doi.org/10.1175/JPO2704.1

Duarte, C. M., Agusti, S., Barbier, E., Britten, G. L., Castilla, J. C., Gattuso, J. P., et al. (2020). Rebuilding marine life. *Nature*, *580*(7801), 39–51. https://doi.org/10.1038/s41586-020-2146-7

Etminan, V., Lowe, R. J., & Ghisalberti, M. (2017). A new model for predicting the drag exerted by vegetation canopies. *Water Resources Research*, *53*(4), 3179–3196. https://doi.org/10.1002/2016WR020090

Finnigan, J. (2000). Turbulence in plant canopies. *Annual Review of Fluid Mechanics*, *32*(1), 519–571. https://doi.org/10.1146/annurev.fluid.32.1.519

Foggi Rota, G., Chiarini, A., & Rosti, M. E. (2025a). Gfr997/CFF-FoggiRotaEtAl2025GRL (v1.2) [Dataset]. *Zenodo*. https://doi.org/10.5281/zenodo.17588891

Foggi Rota, G., Chiarini, A., & Rosti, M. E. (2025b). Reconfiguration and dynamics of clamped fibers under finite-amplitude surface gravity waves. *Physical Review Fluids*, *10*(1), 014301. https://doi.org/10.1103/PhysRevFluids.10.014301

Foggi Rota, G., Koseki, M., Agrawal, R., Olivieri, S., & Rosti, M. E. (2024). Forced and natural dynamics of a clamped flexible fiber in wall turbulence. *Physical Review Fluids*, *9*(1), L012601. https://doi.org/10.1103/PhysRevFluids.9.L012601

Foggi Rota, G., Monti, A., Olivieri, S., & Rosti, M. E. (2024). Dynamics and fluid–structure interaction in turbulent flows within and above flexible canopies. *Journal of Fluid Mechanics*, *989*, A11. https://doi.org/10.1017/jfm.2024.481

Foggi Rota, G., Tressoldi, E., Avallone, F., & Rosti, M. E. (2025). Edge effects in the turbulent flow over flexible aquatic vegetation. *Journal of Fluid Mechanics*, *1019*, A45. https://doi.org/10.1017/jfm.2025.10629

Gauss, C. F. (1828). *Disquisitiones generales circa superficies curvas*. Typis Dieterichianis.

Ghisalberti, M., & Nepf, H. (2006). The structure of the shear layer in flows over rigid and flexible canopies. *Environmental Fluid Mechanics*, *6*(3), 277–301. https://doi.org/10.1007/s10652-006-0002-4

Ghisalberti, M., & Nepf, H. M. (2002). Mixing layers and coherent structures in vegetated aquatic flows. *Journal of Geophysical Research*, *107*(C2), 3-1–3-11. https://doi.org/10.1029/2001JC000871

Ghisalberti, M., & Nepf, H. M. (2004). The limited growth of vegetated shear layers. *Water Resources Research*, *40*(7). https://doi.org/10.1029/2003WR002776

Giamagas, G., Zonta, F., Roccon, A., & Soldati, A. (2023). Propagation of capillary waves in two-layer oil–water turbulent flow. *Journal of Fluid Mechanics*, *960*, A5. https://doi.org/10.1017/jfm.2023.189

Goda, Y. (1970). *Numerical experiments on wave statistics with spectral simulation (technical note No. 009-03-01). Ministry of Transport, Japan*. The Port and Harbour Research Institute.

Hori, N., Ng, C. S., Lohse, D., & Verzicco, R. (2023). Interfacial-dominated torque response in liquid–liquid Taylor–Couette flows. *Journal of Fluid Mechanics*, *956*, A15. https://doi.org/10.1017/jfm.2023.29

Huang, W. X., Shin, S. J., & Sung, H. J. (2007). Simulation of flexible filaments in a uniform flow by the immersed boundary method. *Journal of Computational Physics*, *226*(2), 2206–2228. https://doi.org/10.1016/j.jcp.2007.07.002

Hwang, P. A. (2022). Ocean surface roughness from satellite observations and spectrum modeling of wind waves. *Journal of Physical Oceanography*, *52*(9), 2143–2158. https://doi.org/10.1175/JPO-D-22-0043.1

Ii, S., Sugiyama, K., Takeuchi, S., Takagi, S., Matsumoto, Y., & Xiao, F. (2012). An interface capturing method with a continuous function: The THINC method with multi-dimensional reconstruction. *Journal of Computational Physics*, *231*(5), 2328–2358. https://doi.org/10.1016/j.jcp.2011.11.038

Jain, S. S., Tyagi, N., Prakash, R. S., Ravikrishna, R. V., & Tomar, G. (2019). Secondary breakup of drops at moderate Weber numbers: Effect of Density ratio and Reynolds number. *International Journal of Multiphase Flow*, *117*, 25–41. https://doi.org/10.1016/j.ijmultiphaseflow.2019.04.026

Jiménez, J. (2004). Turbulent flows over rough walls. *Annual Review of Fluid Mechanics*, *36*(1), 173–196. https://doi.org/10.1146/annurev.fluid.36.050802.122103

Jiménez, J., & Pinelli, A. (1999). The autonomous cycle of near-wall turbulence. *Journal of Fluid Mechanics*, *389*, 335–359. https://doi.org/10.1017/S0022112099005066

Kadivar, M., Tormey, D., & McGranaghan, G. (2021). A review on turbulent flow over rough surfaces: Fundamentals and theories. *International Journal of Thermofluids*, *10*, 100077. https://doi.org/10.1016/j.ijft.2021.100077

Kim, H. D., Yu, X., & Kaplan, D. (2024). Steady flow over a finite patch of submerged flexible vegetation. *Water Resources Research*, *60*(1), e2023WR035222. https://doi.org/10.1029/2023WR035222

Kim, J., & Moin, P. (1985). Application of a fractional-step method to incompressible Navier-Stokes equations. *Journal of Computational Physics*, *59*(2), 308–323. https://doi.org/10.1016/0021-9991(85)90148-2

Kim, J., Moin, P., & Moser, R. (1987). Turbulence statistics in fully developed channel flow at low Reynolds number. *Journal of Fluid Mechanics*, *177*, 133–166. https://doi.org/10.1017/S0022112087000892

Kitaigorodskii, S. A., & Donelan, M. A. (1984). Wind-wave effects on gas transfer. In W. Brutsaert & G. H. Jirka (Eds.), *Gas Transfer at Water Surfaces* (pp. 147–170). Springer Netherlands. https://doi.org/10.1007/978-94-017-1660-4_14

Kobayashi, N., Raichle, A. W., & Asano, T. (1993). Wave attenuation by vegetation. *Journal of Waterway, Port, Coastal, and Ocean Engineering*, *119*(1), 30–48. https://doi.org/10.1061/(ASCE)0733-950X(1993)119:1(30)

Liu, D., Diplas, P., Fairbanks, J. D., & Hodges, C. C. (2008). An experimental study of flow through rigid vegetation. *Journal of Geophysical Research*, *113*(F4). https://doi.org/10.1029/2008JF001042

Löhrer, B., & Fröhlich, J. (2023). Large eddy simulation of the flow over a canopy with spanwise patches. *PAMM*, *23*, e202300256. https://doi.org/10.1002/pamm.202300256

Lorenzo, M., Pezzutto, P., De Lillo, F., Ventrella, F. M., De Vita, F., Bosia, F., & Onorato, M. (2023). Attenuating surface gravity waves with an array of submerged resonators: An experimental study. *Journal of Fluid Mechanics*, *973*, A16. https://doi.org/10.1017/jfm.2023.741

Marjoribanks, T. I., Hardy, R. J., Lane, S. N., & Parsons, D. R. (2017). Does the canopy mixing layer model apply to highly flexible aquatic vegetation? Insights from numerical modelling. *Environmental Fluid Mechanics*, *17*(2), 277–301. https://doi.org/10.1007/s10652-016-9482-z

Mei, C. C., Chan, I. C., Liu, L. F., Huang, Z., & Zhang, W. (2011). Long waves through emergent coastal vegetation. *Journal of Fluid Mechanics*, *687*, 461–491. https://doi.org/10.1017/jfm.2011.373

Monti, A., Olivieri, S., & Rosti, M. E. (2023). Collective dynamics of dense hairy surfaces in turbulent flow. *Scientific Reports*, *13*(1), 5184. https://doi.org/10.1038/s41598-023-31534-7

Monti, A., Omidyeganeh, M., Eckhardt, B., & Pinelli, A. (2020). On the genesis of different regimes in canopy flows: A numerical investigation. *Journal of Fluid Mechanics*, *891*, A9. https://doi.org/10.1017/jfm.2020.155

Monti, A., Omidyeganeh, M., & Pinelli, A. (2019). Large-eddy simulation of an open-channel flow bounded by a semi-dense rigid filamentous canopy: Scaling and flow structure. *Physics of Fluids*, *31*(6), 065108. https://doi.org/10.1063/1.5095770

Mossa, M., & De Padova, D. (2025). Interaction between waves and vegetation. *Scientific Reports*, *15*(1), 6157. https://doi.org/10.1038/s41598-025-89627-4

Nepf, H. M. (2012). Flow and transport in regions with aquatic vegetation. *Annual Review of Fluid Mechanics*, *44*(1), 123–142. https://doi.org/10.1146/annurev-fluid-120710-101048

Nepf, H. M., & Vivoni, E. R. (2000). Flow structure in depth-limited, vegetated flow. *Journal of Geophysical Research*, *105*(C12), 28547–28557. https://doi.org/10.1029/2000JC900145

Nikuradse, J. (1933). *Strömungsgesteze in Rauhen Rohren* (Vol. 361). VDI Forsch.

Olivieri, S., Brandt, L., Rosti, M. E., & Mazzino, A. (2020). Dispersed fibers change the classical energy budget of turbulence via nonlocal transfer. *Physical Review Letters*, *125*(11), 114501. https://doi.org/10.1103/PhysRevLett.125.114501

Park, H., & Nepf, H. (2025). Turbulence in a channel with a patchy submerged canopy: The impact of spatial configuration. *Journal of Fluid Mechanics*, *1006*, A15. https://doi.org/10.1017/jfm.2025.12

Poggi, D., Porporato, A., Ridolfi, L., Albertson, J. D., & Katul, G. G. (2004). The effect of vegetation density on canopy sub-layer turbulence. *Boundary-Layer Meteorology*, *111*(3), 565–587. https://doi.org/10.1023/B:BOUN.0000016576.05621.73

Pope, S. B. (2000). *Turbulent flows*. Cambridge University Press.

Popinet, S. (2018). Numerical models of surface tension. *Annual Review of Fluid Mechanics*, *50*(1), 49–75. https://doi.org/10.1146/annurev-fluid-122316-045034

Rigon, G., Albertazzi, B., Mabey, P., Michel, T., Falize, E., Bouffetier, V., et al. (2021). Exploring the Atwood-number dependence of the highly nonlinear Rayleigh-Taylor instability regime in high-energy-density conditions. *Physical Review E - Statistical Physics, Plasmas, Fluids, and Related Interdisciplinary Topics*, *104*(4), 045213. https://doi.org/10.1103/PhysRevE.104.045213

Rosti, M. E., De Vita, F., & Brandt, L. (2019). Numerical simulations of emulsions in shear flows. *Acta Mechanica*, *230*(2), 667–682. https://doi.org/10.1007/s00707-018-2265-5

Sathe, A. S., & Giometto, M. G. (2024). Impact of the numerical domain on turbulent flow statistics: Scalings and considerations for canopy flows. *Journal of Fluid Mechanics*, *979*, A36. https://doi.org/10.1017/jfm.2023.1041

Shimizu, Y., Tsujimoto, T., Nakagawa, H., & Kitamura, T. (1992). Experimental study on flow over rigid vegetation simulated by cylinders with equi-spacing. *Doboku Gakkai Ronbunshu*, *447/II-19*, 35–44.

Sullivan, P. P., McWILLIAMS, J. C., & Moeng, C. H. (2000). Simulation of turbulent flow over idealized water waves. *Journal of Fluid Mechanics*, *404*, 47–85. https://doi.org/10.1017/S0022112099006965

Tang, C., Jia, H., Zhang, S., Yi, Y., & Dey, S. (2025). Hydrodynamics of turbulent flow in channels with submerged flexible vegetation canopy. *Physics of Fluids*, *37*(3), 032123. https://doi.org/10.1063/5.0263237

Taylor, P. K., & Yelland, M. J. (2000). On the apparent "imbalance" term in the turbulent kinetic energy budget. *Journal of Atmospheric and Oceanic Technology*, *17*(1), 82–89. https://doi.org/10.1175/1520-0426(2000)017⟨0082:OTAITI⟩2.0.CO;2

Toba, Y. (1972). Local balance in the air-sea boundary processes. *Journal of the Oceanographical Society of Japan*, *28*(3), 109–120. https://doi.org/10.1007/BF02109772

van Rooijen, A., Lowe, R., Ghisalberti, M., Conde-Frias, M., & Tan, L. (2018). Predicting current-induced drag in emergent and submerged aquatic vegetation canopies. *Frontiers in Marine Science*, *5*, 449. https://doi.org/10.3389/fmars.2018.00449

Winiarska, E., Liberzon, D., & van Hout, R. (2024). Flow field characteristics at the spanwise edge of a vegetative canopy model. *Boundary-Layer Meteorology*, *190*(10), 40. https://doi.org/10.1007/s10546-024-00881-x

Wu, W. C., & Cox, D. T. (2015). Effects of wave steepness and relative water depth on wave attenuation by emergent vegetation. *Estuarine, Coastal and Shelf Science*, *164*, 443–450. https://doi.org/10.1016/j.ecss.2015.08.009

Yang, D., Meneveau, C., & Shen, L. (2013). Dynamic modelling of sea-surface roughness for large-eddy simulation of wind over ocean wavefield. *Journal of Fluid Mechanics*, *726*, 62–99. https://doi.org/10.1017/jfm.2013.215

Yoshimura, H., Omori, Y., & Fujita, I. (2024). Numerical investigation of wind stress on surface velocity and vertical velocity profile in an open-channel flow. *Journal of JSCE*, *12*(2). https://doi.org/10.2208/journalofjsce.23-16165

Zhang, X., & Nepf, H. (2021). Wave damping by flexible marsh plants influenced by current. *Physical Review Fluids*, *6*(10), 100502. https://doi.org/10.1103/PhysRevFluids.6.100502

Zhao, T., & Nepf, H. M. (2021). Turbulence dictates bedload transport in vegetated channels without dependence on stem diameter and arrangement. *Geophysical Research Letters*, *48*(21), e2021GL095316. https://doi.org/10.1029/2021GL095316

Zhu, L., & Chen, Q. (2019). Phase-averaged drag force of nonlinear waves over submerged and through emergent vegetation. *Journal of Geophysical Research: Oceans*, *124*(7), 4368–4388. https://doi.org/10.1029/2018JC014867

Zhu, L., Huguenard, K., Fredriksson, D. W., & Lei, J. (2022). Wave attenuation by flexible vegetation (and suspended kelp) with blade motion: Analytical solutions. *Advances in Water Resources*, *162*, 104148. https://doi.org/10.1016/j.advwatres.2022.104148